Orbitally selective breakdown of the Fermi liquid and simultaneous enhancement of metallic and insulating states in correlated multiband systems with spin-orbit coupling

Ze-Yi Song, Xiu-Cai Jiang, and Yu-Zhong Zhang [*]

Shanghai Key Laboratory of Special Artificial Microstructure Materials and Technology,
School of Physics Science and Engineering, Tongji University,
Shanghai 200092, People's Republic of China

We show that spin-orbit coupling (SOC) plays Janus-faced roles on the orbitally selective Mott transitions in a three-orbital Hubbard model with crystal field splitting at a specific filling of 2/3, which is a minimal Hamiltonian for ruthenates. While the SOC favors the metallic state due to enhancement of orbital hybridization at smaller on-site Coulomb repulsions, it stabilizes the Mott-insulating state ascribed to the lifting of orbital degeneracies and enhancement of band polarizations at larger electronic interaction. Moreover, an orbitally selective non-Fermi liquid (OSNFL), where breakdown and retention of the Fermi liquid coexist in different orbitals, emerges between the orbitally selective Mott phase and the Fermi-liquid state. This novel state can be used to account for the exotic metallic behavior observed in $4d$ materials, such as $Ca_{1.8}Sr_{0.2}RuO_4$, Ba_2RuO_4 under strain, and Sr_2RuO_4 under uniaxial pressure. We propose that orbitally selective Kondo breakdown may account for the OSNFL.

I. INTRODUCTION

Multiorbital correlated electronic systems have been extensively investigated for decades since the discoveries of iron-based superconductors [1,2] and $4d$, $5d$ materials like ruthenates and iridates [3–5], etc. The interplay of factors like the kinetic energy, crystal field splitting, spin-orbit coupling (SOC), Hund's rule coupling, and the Hubbard interaction dominates various exotic properties of these systems. For example, sizable SOC and Coulomb repulsion in $4d$ and $5d$ materials [5] leads to unconventional superconductivity [6,7], SOC-assisted Mott transition [8–13], quantum spin liquids [14], spin-orbit exciton condensation [15,16], and exotic magnetic order [15,17–19]. Among all the phenomena mentioned above, SOC-assisted Mott transition is of particular interest, where the SOC lifts orbital degeneracy, resulting in an effective half-filled system. Then, the Mott transition occurs at intermediate Coulomb interaction, as observed in Sr_2IrO_4 [8].

Meanwhile, the Hund's rule coupling served as a band decoupler [20], together with the crystal field splitting, which lowers the orbital degeneracy, opening a promising way to generate orbital selectivity which is believed to widely exist in ruthenates [21–28] and iron-based superconductors [21,29–33]. The corresponding metallic state, the so-called Hund's metal, with electronic correlations dominated by Hund's coupling, rather than the Hubbard interaction, is of current intense interest since it may be responsible for exotic metallic behavior [21] and unconventional superconductivity [29]. Under certain circumstances [34–38], the orbitally

selective Mott (OSM) transition [39] takes place, where partial bands become Mott insulating and the others remain metallic.

However, comprehensive understanding of quantum phase transitions in real materials with multiple active orbitals is still missing [22,27,39–41] since the SOC and the crystal field splitting are always separately taken into account [42–46] when the electronic correlations are theoretically treated within some reliable approximations like the dynamical mean-field theory (DMFT) [47]. Such unrealistic modeling may result in misleading of the effect of SOC on Hund's metals, the orbital selectivity, and Mott insulators.

In this paper, we study a three-orbital Hubbard model to investigate the influence of SOC on the orbital-differentiated correlations induced by both the lifted degeneracies due to the crystal field splitting and the orbital decoupling ascribed to Hund's coupling at zero temperature. The main results are schematically summarized in Fig. 1. In the absence of SOC, two phases are identified within the interacting range we studied, including the Fermi-liquid state and the OSM state. The SOC is found to effectively suppress the electronic correlations at small Coulomb interaction and favor the Fermi-liquid state. The competition between SOC and electronic correlations leads to the emergence of an exotic metallic state [48], characterized by the coexistence of the Fermi-liquid state and non-Fermi-liquid state in different orbitals, which can account for orbitally selective breakdown of the Fermi liquid observed in $Ca_{1.8}Sr_{0.2}RuO_4$ by recent angle-resolved photoemission spectroscopy experiments [27] and early transport measurements [49]. In contrast, the SOC enhances electronic correlations at large Coulomb repulsion and results in reduced critical values of phase transitions from the OSM state to the Mott insulator.
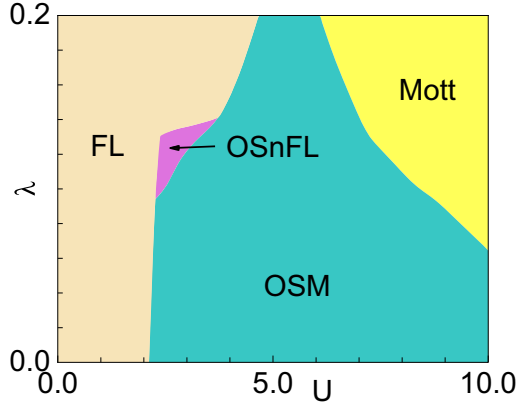
*Corresponding author: yzzhang@tongji.edu.cn

FIG. 1. The schematic phase diagram for the three-orbital Hubbard model in the plane of λ and U. FL, OSM, OSNFL, and Mott denote the Fermi liquid, orbitally selective Mott phase, orbitally selective non-Fermi liquid, and Mott insulator, respectively.

II. MODEL AND METHOD

To obtain the above phase diagram, the three-orbital Hubbard model on the Bethe lattice is considered, which is defined as

$$
\begin{aligned}
H = {} & t \sum_{\langle ij\rangle\alpha\sigma} C_{i\alpha\sigma}^{\dagger} C_{j\alpha\sigma} + \sum_{i\alpha\sigma}(\Delta_{\alpha} - \mu)n_{i\alpha\sigma} \\
& + U \sum_{i\alpha} n_{i\alpha\uparrow} n_{i\alpha\downarrow} + (U' - J_z)\sum_{i\alpha>\beta\sigma} n_{i\alpha\sigma}n_{i\beta\sigma} \\
& + U' \sum_{i\alpha>\beta\sigma} n_{i\alpha\sigma}n_{i\beta\bar\sigma} - J_f \sum_{i\alpha>\beta}[S_{i\alpha}^{+}S_{i\beta}^{-} + S_{i\alpha}^{-}S_{i\beta}^{+}] \\
& + J_p \sum_{i\alpha\neq\beta} C_{i\alpha\uparrow}^{\dagger}C_{i\alpha\downarrow}^{\dagger}C_{i\beta\downarrow}C_{i\beta\uparrow} + H_{\text{SOC}}, \qquad (1)
\end{aligned}
$$

where t denotes the nearest-neighbor hopping, Δ_{α} represents crystal field splitting for the t_{2g} basis with orbital indices $\alpha = \{yz, xz, xy\}$, and μ is the chemical potential. U and U' are the on-site intraorbital and interorbital Coulomb repulsions, respectively. Hund's rule couplings consist of the Ising-type coupling J_z, the spin-flip term J_f, and the pair-hopping term J_p. The relationship $U = U' + 2J_z$ is employed to ensure the electronic interaction is rotationally invariant. $C_{i\alpha\sigma}^{\dagger}$ ($C_{i\alpha\sigma}$) creates (annihilates) an electron with spin σ in orbital α of lattice site i. S and n represent the spin and particle number operators, respectively. The relativistic SOC reads

$$
H_{\text{SOC}} = \lambda \sum_{i\alpha\beta} \sum_{\sigma_1\sigma_2}\langle\alpha|\mathbf{L}_i|\beta\rangle\langle\sigma_1|S_i|\sigma_2\rangle C_{i\alpha\sigma_1}^{\dagger}C_{i\beta\sigma_2}, \qquad (2)
$$

where λ is the strength of the SOC and $\mathbf{L}$ is the local orbital angular momentum operator. The matrix representations of $L = 2$ in the t_{2g} basis are the same as the ones for $L = 1$ in the cubic basis except for a sign in accordance with the T-P correspondence [5,50].

We employed the DMFT in combination with exact diagonalization (ED) [47] as an impurity solver to solve the model (1) on the Bethe lattice with infinite coordinates at a filling of $n = 2/3$, namely, four electrons in three orbitals, and at zero temperature. The noninteracting density of states
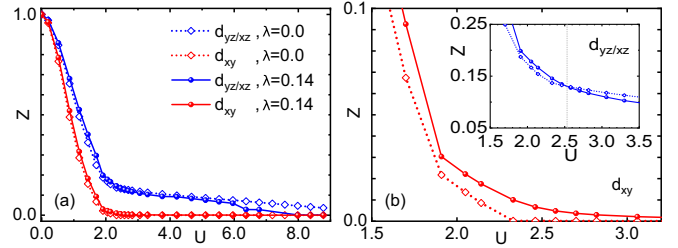

FIG. 2. (a) The quasiparticle residue Z of t_{2g} orbitals as a function of U at $\lambda = 0.0$ and $\lambda = 0.14$. (b) Blowup for Z of the d_{xy} orbital near the critical point $U_{xy}^c(\lambda = 0.0)$ of about 2.3; those for $d_{yz/xz}$ orbitals are shown in the inset.

is $\rho_{\alpha}(\omega) = \frac{2}{\pi D^2}\sqrt{D^2 - \omega^2}$, and the half bandwidth D is used as the energy unit. The effective inverse temperature was set to $\beta D = 200$, which serves as a low-frequency cutoff. On the Bethe lattice, the DMFT self-consistent conditions simply read $\hat{\Delta}(\omega) = \frac{D^2}{4}\hat{G}(\omega)$, where $\hat{\Delta}(\omega)$ is a matrix for hybrid functions and $\hat{G}(\omega)$ is a matrix for local lattice Green's functions. In total six baths were used to fit the hybrid function $\hat{\Delta}(\omega)$. In our calculations, the orbital degeneracy is lifted by crystal field splitting (i.e., $\Delta_{yz} = \Delta_{xz} \neq \Delta_{xy}$), leading to a nondegenerate d_{xy} orbital and doubly degenerate $d_{yz/xz}$ orbitals. We fix electronic populations to be (1.5,1.5,1.0) in accordance with that of $Ca_{1.8}Sr_{0.2}RuO_4$ [27] in the absence of SOC, which can be realized by tuning the orbitally dependent potential Δ_{α} [36]. The calculations were performed in the paramagnetic state with isotropic Hund's coupling where $J_z = J_f = J_p$. The broadening factor $\eta = 0.02D$ is used to calculate real-frequency dynamical quantities, including the Green's functions, self-energies, and dynamical susceptibilities for spin, orbital, and total angular momenta.

III. RESULTS

In order to explore the influence of SOC on the electronic correlations in multiband systems, we have calculated the quasiparticle residue $Z_{\alpha} = (1 - \frac{\partial \text{Re}\Sigma_{\alpha}(\omega)}{\partial\omega}|_{\omega\to 0})^{-1}$, as shown in Fig. 2(a), where $\text{Re}\Sigma_{\alpha}(\omega)$ is the real part of the self-energies of t_{2g} orbitals. In the absence of SOC, Z_{xy} is rapidly suppressed as U increases and vanishes at a critical value of $U_{xy}^c(\lambda = 0.0) \approx 2.3$, indicating a Mott-Hubbard gap opens in the d_{xy} band. In contrast, although $Z_{yz/xz}$ is drastically reduced at the beginning, it remains finite in a wide region of U with $U_{yz/xz}^c(\lambda = 0.0)$ being much larger than $U_{xy}^c(\lambda = 0.0)$, which suggests an occurrence of the OSM phase where electrons in the d_{xy} band become Mott localized and those in $d_{yz/xz}$ bands remain itinerant. This is in excellent agreement with previous results [36].

When the SOC is taken into account, e.g., $\lambda = 0.14$, the quasiparticle residues behave distinctly at small and large Coulomb repulsions in comparison to those at $\lambda = 0.0$. At large U, the SOC enhances the electronic correlations in $d_{yz/xz}$ bands, as indicated by suppression of $Z_{yz/xz}$, leading to a smaller critical value of Mott transition $U_{yz/xz}^c(\lambda = 0.14)$ than that of the $\lambda = 0.0$ case. Since the Mott-insulating state with a vanishing Z_{xy} remains in the d_{xy} band, it suggests that the SOC cooperates with the Coulomb interaction and stabilizes the
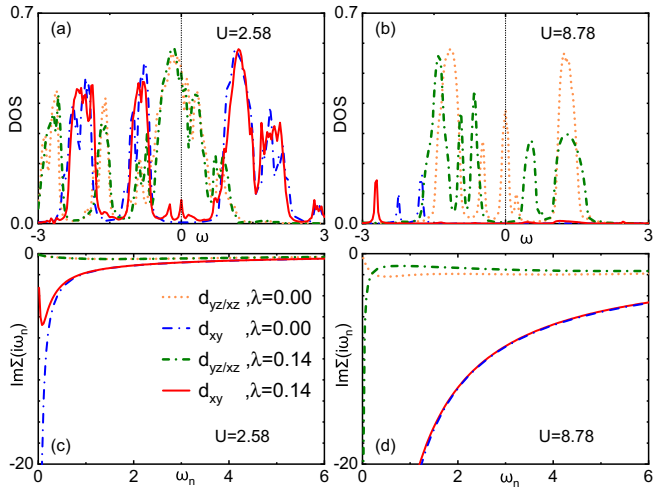
FIG. 3. (a) and (b) Density of states projected onto the t_{2g} orbitals and (c) and (d) the imaginary part of the self-energy on the Matsubara axis at $U = 2.58$ and $U = 8.78$ for $\lambda = 0.0$ and $\lambda = 0.14$.
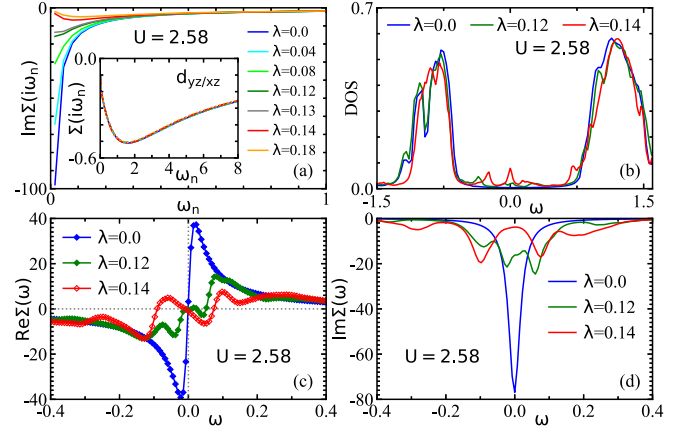

FIG. 4. (a) The influence of spin-orbit coupling on the imaginary part of Matsubara self-energy for the d_{xy} band; those for $d_{yz/xz}$ bands are shown in the inset. (b) Density of states for the d_{xy} band in the Mott ($\lambda = 0.0$), non-Fermi-liquid ($\lambda = 0.12$), and Fermi-liquid ($\lambda = 0.14$) states. (c) Real and (d) imaginary parts of self-energy of the d_{xy} band on the real-frequency axis. Here, the electron repulsion is fixed at $U = 2.58$.

Mott-insulating ground state. Conversely, at small U, the SOC suppresses the electronic correlations in all bands, as inferred by larger values of Z in comparison to those for the $\lambda = 0$ case, as shown in Fig. 2(b), which is a blowup of Fig. 2(a) in the small-U region. This gives rise to an intersection of $Z_{yz/xz}$ between the $\lambda = 0.14$ and $\lambda = 0.0$ cases at $U \approx 2.5$, as seen in the inset of Fig. 2(b). Furthermore, the quasiparticle residue Z_{xy} of the $\lambda = 0.14$ case remains nonzero for a wide range of $U > U_{xy}^c(\lambda = 0.0)$, suggesting that a transition from a Mott insulator to a metal may take place in the d_{xy} band when SOC is turned on. This indicates that the SOC competes with the on-site Coulomb repulsion and favors a metallic ground state at small U. Obviously, the SOC shows opposite effects on the Mott transitions in multiband systems.

We further demonstrate the pronounced effects of the SOC in the vicinity of phase transitions in Fig. 3, where the calculated density of states projected onto the t_{2g} basis and corresponding imaginary part of the Matsubara self-energy $\text{Im}\Sigma_\alpha(i\omega_n)$ are exhibited. In the absence of the SOC, at both $U = 2.58$ and $U = 8.78$, the density of states at the Fermi level vanishes in the d_{xy} orbital, and $\text{Im}\Sigma_{xy}(i\omega_n)$ diverges in proximity to zero frequency, which is a typical character of a Mott insulator. Meanwhile, the $d_{yz/xz}$ orbitals behave as Fermi liquids since the density of states is finite at $\omega = 0$ and $\text{Im}\Sigma_{yz/xz}(i\omega_n)$ approaches zero at low frequency. These results suggest that the system is in the OSM phase. When λ increases to 0.14, the SOC exhibits distinct effects at small and large U. At $U = 8.78$, while the SOC barely influences the nature of the d_{xy} orbital, the complete suppression of the density of states of $d_{yz/xz}$ orbitals at the Fermi level and the divergence of $\text{Im}\Sigma_{yz/xz}(i\omega_n)$ as ω_n goes to zero suggest the appearance of the SOC-assisted Mott phase. On the other hand, at $U = 2.58$, the SOC drastically affects the properties of the d_{xy} orbital but hardly influences those of $d_{yz/xz}$ orbitals. The appearance of the central peak of the density of states for the d_{xy} orbital at the Fermi level and $\text{Im}\Sigma_{xy}(i\omega_n)$ extrapolating to zero as $\omega_n \to 0$ suggests a SOC-induced Fermi-liquid behavior.

The occurrence of the SOC-assisted Mott phase at large U can be easily understood within the $|J, \pm m\rangle$ basis, where the local Hamiltonian (2) can be diagonalized. Here, J denotes the total angular momentum, and $\pm m$ represents its projection in the z direction. It is found that the SOC enhances band polarizations and leads to a full occupation of the $|\frac{3}{2}, \pm\frac{3}{2}\rangle$ bands at λ_c of about 0.1. Then, the other two electrons reside in the $|\frac{3}{2}, \pm\frac{1}{2}\rangle$ and $|\frac{1}{2}, \pm\frac{1}{2}\rangle$ bands, resulting in an effective half-filled system, rather than the original four electrons per three orbitals. Therefore, the SOC favors Mott transition at large U since the effective filling is changed.

On the contrary, in the small-U region, an OSM phase requires decoupling between the Mott-insulating d_{xy} orbital and metallic $d_{yz/xz}$ orbitals, which is originally fulfilled by Hund's rule interaction in the absence of SOC. However, the SOC introduces coupling between the d_{xy} and $d_{yz/xz}$ orbitals, leading to enhancements of both orbital fluctuations and the kinetic energies of all orbitals. Therefore, the SOC tends to destroy the Mott phase of the d_{xy} orbital and favors the metallic state due to the increase of the bandwidth and decrease of band decoupling at small U.

Besides the opposite effect of SOC on electronic correlations, it is also interesting to find an intermediate phase, called the orbitally selective non-Fermi liquid (OSNFL), where breakdown of the Fermi liquid happens only in d_{xy} orbitals, emerging between the Fermi-liquid state and the OSM phase in the small-U and intermediate-λ region, as presented in Fig. 1. This exotic metallic state can be clearly identified by the imaginary part of the Matsubara self-energy $\text{Im}\Sigma_\alpha(i\omega_n)$, as shown in Fig. 4(a). For example, at $U = 2.58$, while $\text{Im}\Sigma_{yz/xz}(i\omega_n)$ always goes to zero as $\omega_n \to 0$, indicating Fermi liquids in $d_{yz/xz}$ bands [see the inset of Fig. 4(a)], $\text{Im}\Sigma_{xy}(i\omega_n)$ extrapolates to a finite value as $\omega_n \to 0$ around $\lambda \approx 0.12$, which is in sharp contrast to the divergent behavior for $\lambda \leqslant 0.08$ and the tendency to approach zero for
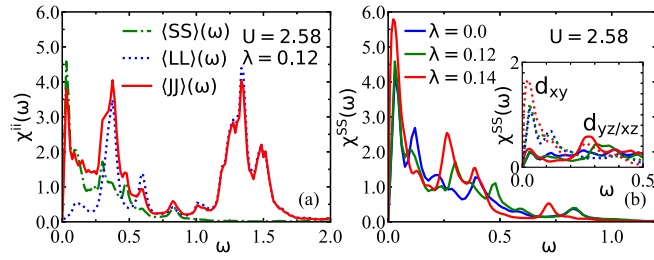
FIG. 5. (a) Dynamical susceptibilities for spin (**S**), orbital (**L**), and total (**J**) angular momenta at $U = 2.58$ and $\lambda = 0.12$. (b) Dynamical spin susceptibilities at $U = 2.58$ for the $\lambda = 0.0$, $\lambda = 0.12$, and $\lambda = 0.14$ cases; the inset shows corresponding orbitally resolved dynamical spin susceptibilities, where solid lines denote $d_{yz/xz}$ orbitals and dashed lines denote the d_{xy} orbital.

$\lambda \geqslant 0.14$. The finite scattering rate suggests a finite lifetime of quasiparticles and a breakdown of the Fermi liquid at zero temperature.

The self-energy $\Sigma_{xy}(\omega)$ on the real-frequency axis again reveals the SOC-induced non-Fermi-liquid behavior in d_{xy} band. Figures 4(c) and 4(d) show the real part of the self-energy $\mathrm{Re}\,\Sigma_{xy}(\omega)$ and imaginary part of the self-energy $\mathrm{Im}\,\Sigma_{xy}(\omega)$ at $U = 2.58$ for $\lambda = 0.0$, $\lambda = 0.12$, and $\lambda = 0.14$. When $\lambda = 0.12$, the positive slop of $\mathrm{Re}\,\Sigma_{xy}(\omega)$ at the Fermi level and the finite $\mathrm{Im}\,\Sigma_{xy}(\omega)$ suggest the breakdown of the quasiparticle picture. The development of additional low-energy poles of $\omega + \mu - \varepsilon - \mathrm{Re}\,\Sigma_{xy}(\omega) = 0$ close to the Fermi level and the finite scattering rate at $\omega = 0$ lead to the appearance of a pseudogap in the d_{xy} band, as depicted in Fig. 4(b), reminiscent of that observed in the Hubbard model within cluster DMFT [51]. This is strikingly different from those for $\lambda = 0.0$ and 0.14. For the former, the divergent $\mathrm{Im}\,\Sigma_{xy}(\omega)$ at $\omega = 0$ and the steep positive slop of $\mathrm{Re}\,\Sigma_{xy}(\omega)$ suggest a Mott-insulating state. In contrast, for the latter, $\mathrm{Im}\,\Sigma_{xy}(\omega)$ can be fitted by ω^2, and $\mathrm{Re}\,\Sigma_{xy}(\omega)$ is linearly ω dependent, indicating a typical Fermi-liquid behavior at zero temperature. Figure 4(b) shows the density of states for the d_{xy} band in the Mott, pseudogap, and Fermi-liquid states at $\lambda = 0.00$, 0.12, and 0.14, respectively.

Now we discuss the underlying physics for the OSNFL state. Since the nature of correlated metals is controlled by the low-energy excitations in the absence of SOC for multiband systems [52,53], we performed similar calculations for the dynamical susceptibilities $\chi^{ii}(\omega)$ of total, orbital, and spin angular momenta, with $i = J$, L, and S, respectively, at $U = 2.58$ and $\lambda = 0.12$, as shown in Fig. 5(a). The dynamical spin susceptibilities are defined as

$$\chi^{SS}(t) = -i\theta(t)\langle|[S(t), S]_-|\rangle, \qquad (3)$$

where $\theta(t)$ is a step function, $|\cdot\rangle$ is the ground state, $[\cdot]_-$ denotes the commutator of two operators, and S is the operator of total spin angular momenta. After performing a Fourier transformation, we obtain

$$\chi^{SS}(z = \omega + i\eta) = -\mathrm{Im}\int_{-\infty}^{\infty} dt\, e^{izt} \chi^{SS}(t). \qquad (4)$$

We display only the imaginary parts since the real parts can be reproduced by the Kramers-Kronig relations. The dynamical

susceptibilities $\chi^{LL}(\omega)$ and $\chi^{JJ}(\omega)$ for the corresponding orbital and total angular momenta can be obtained similarly. The calculation details regarding dynamical correlations are given in Appendix B. From Fig. 5(a), it is found that the low-energy excitations mainly come from spin fluctuations, while the high-energy parts are ascribed to the excitations of orbital momentum **L**. Thus, we focus on analyses of dynamical spin susceptibilities $\chi^{SS}(\omega)$ at $U = 2.58$ for $\lambda = 0.0$, 0.12, and 0.14. At $\lambda = 0.0$, the system is in the OSM phase. The low-energy spin fluctuations consist of two parts; one is attributed to the Kondo screening of spins in $d_{yz/xz}$ bands by itinerant electrons, and the other is ascribed to the existence of spin triplets formed by four electrons in three t_{2g} orbitals [52,53]. At $\lambda = 0.14$, the system becomes a Fermi liquid. The intensity of low-energy spin excitations is drastically enhanced. Since the low-energy spin excitations of $d_{yz/xz}$ bands remain almost unchanged for different λ, as seen in the inset of Fig. 5(b), the abrupt increase should be ascribed to additional Kondo resonances between spins in the d_{xy} band and itinerant electrons. At $\lambda = 0.12$, while electrons in the d_{xy} band become itinerant, the corresponding low-energy spin excitations are similar to those for $\lambda = 0.0$, indicating that the spins in the d_{xy} band do not take part in the Kondo screening. The lack of Kondo screening in the d_{xy} band leads to the emergence of the non-Fermi liquid. Hence, we conclude that the OSNFL state is a result of orbitally selective Kondo breakdown.

IV. DISCUSSION

The calculated results show the Janus-faced influence of SOC on the Mott transitions in the presence of crystal field splitting at a filling of $n = 2/3$. Owing to the orbital degeneracy lifted by crystal field splitting, the Mott transitions in different orbitals take place separately as U increases. The opposite effect of SOC on the electronic correlations leads to the increase of U_{xy}^c and decrease of $U_{yz/xz}^c$, which is in sharp contrast to previous theoretical results in the absence of crystal field splitting, where a common Mott transition occurs and the critical value of U_c can be increased or decreased only by the SOC for given integer fillings [44–46]. Furthermore, the competition between SOC and Coulomb repulsion results in the OSNFL state, characterized by the coexistence of the Fermi liquid and non-Fermi liquid in different orbitals, which is fundamentally distinct from the case of $\lambda = 0.0$, where the metallic ground state is always a Fermi liquid, as displayed in Fig. 1. The coexisting region is of particular importance as it provides a unique platform to study the breakdown of the Fermi-liquid picture and the nature of the non-Fermi-liquid state. The appearance of the OSNFL state requires remarkable orbital-differentiated correlations and sizable orbital hybridizations, reminiscent of the non-Fermi liquid obtained within cluster DMFT [51,54] where multiple sites correspond to multiple orbitals. In addition, we suppose that the non-Fermi liquid might be the collective excitations of spin-charge separation.

Next, we discuss the relevance of our results to real materials. $Ca_{1.8}Sr_{0.2}RuO_4$ satisfies the conditions for the OSNFL state. On the one hand, the intermediate SOC has been observed in Sr_2RuO_4 [55] and Ca_2RuO_4 [56,57]. On the other

hand, $Ca_{1.8}Sr_{0.2}RuO_4$ shows significant orbital-differentiated correlations with effective mass for a d_{xy} band much larger than that for $d_{yz/xz}$ bands [27,40]. Furthermore, enhanced crystal field splitting induced by lattice distortion is detected in $Ca_{1.8}Sr_{0.2}RuO_4$ [58]. Although the material-realistic DMFT calculations claimed that SOC hardly affects the correlations in Sr_2RuO_4 [59] and Ca_2RuO_4 [60], we still suppose that $Ca_{1.8}Sr_{0.2}RuO_4$ should be susceptible to the SOC due to its proximity to the Mott transition. Hence, orbitally selective breakdown of the Fermi liquid observed experimentally in $Ca_{1.8}Sr_{0.2}RuO_4$ [27] may be a result of competition between SOC and orbital-differentiated correlations. Moreover, the non-Fermi liquid caused by strain in Ba_2RuO_4 [61] and uniaxial pressure in Sr_2RuO_4 [62] may also be attributed to the competition since both strain and uniaxial pressure slightly affect $d_{yz/xz}$ bands but significantly increase the renormalization mass of the d_{xy} band due to the band flattening, resulting in enhanced orbital differentiation. In addition, the OSNFL picture may have important implication for understanding the low-temperature non-Fermi liquid in $CaRuO_3$ [63–67].

V. CONCLUSION

In conclusion, we have investigated the three-orbital Hubbard model with both SOC and crystal field splitting using the DMFT combined with ED at 2/3 filling. The OSM transitions take place as the orbital degeneracy is lifted by crystal field splitting in the absence of SOC. It was found that the SOC plays Janus-faced roles in the OSM transitions. While it suppresses the OSM transition at smaller U, it favors the OSM transition at larger U. The competition between the SOC and electronic correlations leads to the emergence of an OSNFL state, where the Fermi liquid coexists with the non-Fermi liquid. The OSNFL state originates from the orbitally selective Kondo breakdown and can be applied to understand the exotic metals in $4d$ materials.

APPENDIX A: DYNAMICAL MEAN-FIELD THEORY FOR MULTIORBITAL HUBBARD MODELS

The DMFT [47] was employed to investigate the multiorbital Hubbard model (1) on the Bethe lattice with an infinite coordination number, for which the DMFT has already been proved to be exact and the model (1) can be exactly mapped onto an Anderson impurity model with self-consistent conditions $\hat{\Delta}(\omega) = \frac{D^2}{4}\hat{G}(\omega)$, where $\hat{G}(\omega)$ is the matrix of local lattice Green's functions, $\hat{\Delta}(\omega)$ denotes the matrix of hybridization functions for the Anderson impurity model, and D represents the half bandwidth. Note that the hat symbol is used to denote a matrix. When the spin-orbit coupling is considered, it is convenient to do the calculations in the $|J, \tau m\rangle$ basis,

where $J = \{\frac{1}{2}, \frac{3}{2}\}$, $m = \{\frac{1}{2}, \frac{3}{2}\}$, $m \leqslant J$, and $\tau = \pm$, specifying a pair of Kramers doublets m, which are the eigenvectors of the Hamiltonian (2). In this representation, the Anderson impurity model reads

$$
\begin{aligned}
H_{\text{imp}} = &\sum_{k\tau m} \epsilon_{km} C_{k\tau m}^\dagger C_{k\tau m} + \sum_p \hat{E}_p d_p^\dagger d_p + \sum_{pq} \hat{M}_{pq} d_p^\dagger d_q \\
&+ \sum_{kJ\tau m} V_{kJ\tau m}(C_{k\tau m}^\dagger d_{J\tau m} + d_{J\tau m}^\dagger C_{k\tau m}) \\
&+ \frac{1}{4} \sum_{pqst} \tilde{U}_{st}^{pq} d_p^\dagger d_q^\dagger d_s d_t,
\end{aligned}
\tag{A1}
$$

where ϵ_{km} denotes the dispersion relationship of bath electrons, p, q, s, t are the orbital indices of $(J, \tau m)$, $\hat{E}_p$ is the eigenvalue of Hamiltonian (2), $\hat{M}_{pq}$ is the matrix element of crystal field splitting in the $|J, \tau m\rangle$ basis, $V_{kJ\tau m}$ denotes the hybridization between local orbitals on the impurity and bath, and $\tilde{U}_{st}^{pq} = \sum_{\alpha\beta\gamma\delta} U_{\alpha\beta\gamma\delta} \hat{A}_{p\alpha}^* \hat{A}_{q\beta}^* \hat{A}_{s\gamma} \hat{A}_{t\delta}$ is the Coulomb interaction tensor element in the $|J, \tau m\rangle$ representation, where $U_{\alpha\beta\gamma\delta}$ is the Coulomb interaction tensor element in the t_{2g} basis and $\hat{A}$ is the unitary transformation [43] between the t_{2g} and $|J, \tau m\rangle$ bases.

The main tasks of the present DMFT calculations are to solve the Anderson impurity model (A1). We took ED as the impurity solver [47]. In order to solve model (A1) with ED, we have to use a finite number of bath sites to optimally fit the continuous bath. In this paper, in total, six discrete bath sites were adopted to couple to three Kramers doublets, i.e., two bath sites per Kramers doublet. Owing to the presence of orbital mixing between $|\frac{1}{2}, \frac{1}{2}\rangle$ ($|\frac{1}{2}, -\frac{1}{2}\rangle$) and $|\frac{3}{2}, \frac{1}{2}\rangle$ ($|\frac{3}{2}, -\frac{1}{2}\rangle$) orbitals, corresponding cross-orbital hybridization functions, like $\hat{\Delta}_{\frac{1}{2}, \frac{1}{2}; \frac{3}{2}, \frac{1}{2}}$ and $\hat{\Delta}_{\frac{1}{2}, -\frac{1}{2}; \frac{3}{2}, -\frac{1}{2}}$, are considered. From Fig. 6, it is found that the Weiss field $\hat{g}(i\omega_n) = [\hat{\Sigma}(i\omega_n) + \hat{G}^{-1}(i\omega_n)]^{-1}$, with $\hat{\Sigma}(i\omega)$ being the matrix of the self-energy, can be well reproduced by the noninteracting impurity Green's function $\hat{g}_{\text{imp}}(i\omega_n)$ defined by (A3) in the OSM [Figs. 6(a)–6(c)], the OSNFL [Figs. 6(d)–6(f)], and the Fermi-liquid [Figs. 6(g)–6(i)] phases, suggesting that the finite-size effects are negligible and the results presented in the paper are convincing. The procedures of the DMFT calculations in combination with ED as the impurity solver are described below.

Starting from an initial set of bath parameters $\{\epsilon_{km}, V_{kJ\tau m}\}$, we construct the Anderson model (A1). The hybridization function of the corresponding impurity model (A1) is written as

$$
\hat{\Delta}_{J,\tau m; J', \tau m}(i\omega_n) = \sum_k \frac{V_{kJ\tau m} V_{kJ'\tau m}}{i\omega_n - \epsilon_{km}},
\tag{A2}
$$

where $\omega_n = \frac{(2n-1)\pi}{\beta}$ is the Matsubara frequency with a fictitious temperature $\beta D = 200$, which serves as a low-frequency cutoff. The noninteracting impurity Green's function of the Anderson model (A1) is

$$
\hat{g}_{\text{imp}}(i\omega_n) = i\omega_n + \mu - \hat{E} - \hat{M} - \hat{\Delta}^{-1}(i\omega_n).
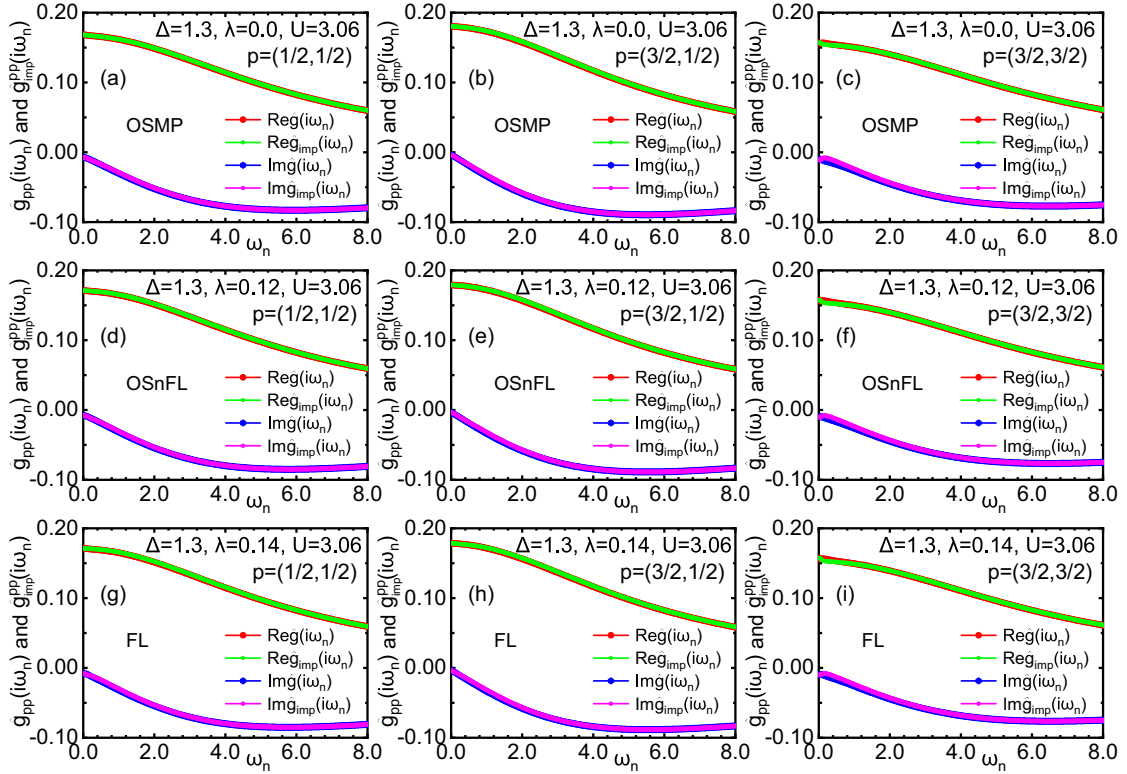\tag{A3}
$$

FIG. 6. Comparison between the Weiss fields $\hat{g}(i\omega_n)$ and the noninteracting impurity Green's functions $\hat{g}_{\mathrm{imp}}(i\omega_n)$ obtained from a discretized Anderson impurity model with six optimal bath sites. $\hat{g}(i\omega_n)$ can be well reproduced by $\hat{g}_{\mathrm{imp}}(i\omega_n)$ in (a)–(c) the OSM, (d)–(f) the OSNFL, and (h)–(i) the Fermi-liquid (FL) phases for all (J, m) orbitals, including $p = (\frac{1}{2}, \frac{1}{2})$, $p = (\frac{3}{2}, \frac{1}{2})$, and $p = (\frac{3}{2}, \frac{3}{2})$ orbitals.

After the impurity Green's function $\hat{G}_{\mathrm{imp}}(i\omega_n)$ is obtained by solving model (A1) with ED, the self-energy $\hat{\Sigma}(i\omega_n)$ can be calculated based on Dyson's equation,

$$\hat{\Sigma}(i\omega_n) = \hat{g}_{\mathrm{imp}}^{-1}(i\omega_n) - \hat{G}_{\mathrm{imp}}^{-1}(i\omega_n). \quad (A4)$$

Finally, the local Green's function of the three-orbital Hubbard model (1) in the $|J, \tau m\rangle$ basis is calculated as

$$\hat{G}(i\omega_n) = \int_{-\infty}^{+\infty} \frac{\rho(\epsilon)d\epsilon}{i\omega_n + \mu - \hat{E} - \hat{M} - \hat{\Sigma}(i\omega_n) - \epsilon}, \quad (A5)$$

where $\rho(\omega) = \frac{2}{\pi D^2}\sqrt{D^2 - \omega^2}$ is the density of states for three Kramers doublets, which is the same as the counterpart for the t_{2g} orbitals. Considering the self-consistent conditions $\hat{\Delta}(i\omega_n) = \frac{D^2}{4}\hat{G}(i\omega_n)$, we can iteratively calculate the local Green's function $\hat{G}(i\omega_n)$ through Eqs. (A1)–(A5).

In our calculations, the parameters $\{\epsilon_{km}, V_{kJ\tau m}\}$ to build the model (A1) are obtained by using the conjugate gradient method to minimize the cost function

$$\chi = \frac{1}{N_{\mathrm{max}}} \sum_{n=1}^{N_{\mathrm{max}}} \frac{1}{\omega_n^2} \sum_{pq} |[\hat{g}(i\omega_n) - \hat{g}_{\mathrm{imp}}(i\omega_n)]_{pq}|, \quad (A6)$$

where $N_{\mathrm{max}} = 256$ is the upper limit of the summation. Starting from a guessed Weiss field $\hat{g}(i\omega_n)$, we can self-consistently obtain the convergent results when the difference Δ_g between the new Weiss field $\hat{g}^{\mathrm{new}}(i\omega_n)$ and the old Weiss field $\hat{g}^{\mathrm{old}}(i\omega_n)$

is less than 10^{-6}. The difference Δ_g is defined as

$$\Delta_g = \max\left\{\left|\hat{g}_{pq}^{\mathrm{new}}(i\omega_n) - \hat{g}_{pq}^{\mathrm{old}}(i\omega_n)\right|\right\}. \quad (A7)$$

Although the present DMFT calculations were performed in the $|J, \tau m\rangle$ basis, the dynamical quantities, like the local lattice Green's function $\hat{G}_{t_{2g}}(i\omega_n)$ and self-energy $\hat{\Sigma}_{t_{2g}}(\omega_n)$, in the t_{2g} basis can be readily obtained via a unitary transformation

$$\hat{G}_{t_{2g}}(i\omega_n) = \hat{A}\hat{G}(i\omega_n)\hat{A}^{\dagger} \quad (A8)$$

and

$$\hat{\Sigma}_{t_{2g}}(i\omega_n) = \hat{A}\hat{\Sigma}(i\omega_n)\hat{A}^{\dagger}. \quad (A9)$$

Since ED has direct access to the real-frequency dynamical correlations as described in Appendix B, we can calculate the local lattice Green's function $\hat{G}(i\omega + i\eta)$ after the self-energy is obtained via the Dyson equation $\hat{\Sigma}(\omega + i\eta) = \hat{g}_{\mathrm{imp}}^{-1}(\omega + i\eta) - \hat{G}_{\mathrm{imp}}^{-1}(\omega + i\eta)$, where the impurity Green's function $\hat{G}_{\mathrm{imp}}(\omega + i\eta)$ is directly produced by ED. Similar to the Matsubara Green's function $\hat{G}_{t_{2g}}(i\omega_n)$, the local Green's function $\hat{G}_{t_{2g}}(\omega + i\eta)$ and self-energy $\hat{\Sigma}_{t_{2g}}(\omega + i\eta)$ in the t_{2g} basis are calculated as

$$\hat{G}_{t_{2g}}(\omega + i\eta) = A\hat{G}(\omega + i\eta)A^{\dagger} \quad (A10)$$

and

$$\hat{\Sigma}_{t_{2g}}(\omega + i\eta) = A\hat{\Sigma}(\omega + i\eta)A^{\dagger}. \quad (A11)$$

On the basis of $\hat{G}_{t_{2g}}(\omega + i\eta)$, the projected density of states, as shown in the main text, is defined as

$$\rho_{\alpha\sigma}(\omega) = -\frac{1}{\pi} \text{Im}[\hat{G}_{t_{2g}}(\omega + i\eta)]_{\alpha\sigma,\alpha\sigma}, \qquad (A12)$$

where α is the orbital index for t_{2g} orbitals and σ denotes electron spin.

APPENDIX B: EXACT DIAGONALIZATION

When ED is employed as an impurity solver of the DMFT, it needs two steps to obtain the dynamical correlation functions. The first step is to calculate the ground-state energy E_g and corresponding eigenvector $|\cdot\rangle$ of the Anderson impurity model (A1) by the Lanczos method. On the basis of the Lanczos method, E_g and $|\cdot\rangle$ can be obtained by iteratively constructing a Krylov space $\{|\phi_n\rangle\}$ from an arbitrary initial configuration $|\phi_1\rangle$ via

$$|\tilde{\phi}_{n+1}\rangle = H_{\text{imp}}|\phi_n\rangle - a_n|\phi_n\rangle - b_n^2|\phi_{n-1}\rangle, \qquad (B1)$$

where $n = 2, 3, 4, \ldots$, $a_n = \langle\phi_n|H_{\text{imp}}|\phi_n\rangle$, $b_n^2 = \langle\tilde{\phi}_{n+1}|\tilde{\phi}_{n+1}\rangle$. Note $|\phi_n\rangle$ denotes a normalized vector, $b_1 = 0$, $|\phi_0\rangle = 0$, $|\tilde{\phi}_2\rangle = H_{\text{imp}}|\phi_1\rangle - a_1|\phi_1\rangle$, and $a_1 = \langle\phi_1|H_{\text{imp}}|\phi_1\rangle$. The iteration (B1) continues until b_n is less than a threshold. In this basis, the Hamiltonian for the Anderson impurity model (A1) is a tridiagonal matrix and simply reads

$$\begin{bmatrix} a_1 & b_2 & 0 & 0 & \cdots \\ b_2 & a_2 & b_3 & 0 & \cdots \\ 0 & b_3 & a_3 & b_4 & \cdots \\ 0 & 0 & b_4 & a_4 & \cdots \\ \vdots & \vdots & \vdots & \vdots & \end{bmatrix}, \qquad (B2)$$

which can be diagonalized by the modern standard library subroutines.

The second step is to calculate the dynamical correlation function based on the ground-state energy E_g and ground-state eigenvector $|\cdot\rangle$ obtained in the first step. For the given operator O, the real-time dynamical correlation function is defined as

$$C_{\alpha\beta}(t) = -i\theta(t)\langle|[O_\alpha(t), O_\beta]_\xi|\rangle, \qquad (B3)$$

where $\theta(t)$ is a step function of time t, $O_\alpha(t) = e^{iH_{\text{imp}}t}O_\alpha e^{-iH_{\text{imp}}t}$, $[\cdot]_\xi$ denotes the commutator of two operators, $\xi = 1$ if O is a Fermi operator, and $\xi = -1$ otherwise. After performing a Fourier transformation, the dynamical correlation function on the real-frequency axis can be written as

$$C_{\alpha\beta}(\omega + i\eta) = C_{\alpha\beta}^>(\omega + i\eta) + \xi C_{\alpha\beta}^<(\omega + i\eta), \qquad (B4)$$

where η is a broadening factor and

$$C_{\alpha\beta}^>(\omega + i\eta) = \langle|O_\alpha \frac{1}{\omega - H_{\text{imp}} + E_g + i\eta} O_\beta|\rangle, \qquad (B5)$$

$$C_{\alpha\beta}^<(\omega + i\eta) = \langle|O_\beta \frac{1}{\omega + H_{\text{imp}} - E_g + i\eta} O_\alpha|\rangle. \qquad (B6)$$

Similar to calculating the ground-state energy E_g and eigenvector $|\cdot\rangle$, the method of the Krylov space can be applied to calculate both dynamical correlation functions above.

In order to calculate $C_{\alpha\beta}^>(\omega + i\eta)$, we start the Lanczos iterations with the initial vector $|\phi_1^\beta\rangle = O_\beta|\rangle/\langle|O_\beta^\dagger O_\beta|\rangle$ to construct the new basis $\{|\phi_n^\beta\rangle\}$. Inserting the completeness $\sum_n |\phi_n^\beta\rangle\langle\phi_n^\beta| = 1$ into Eq. (B5) yields

$$C_{\alpha\beta}^>(\omega + i\eta) = \sqrt{\langle|O_\alpha O_\alpha^\dagger|\rangle}\sqrt{\langle|O_\beta^\dagger O_\beta|\rangle}$$
$$\times \sum_n U_n^{\alpha\beta} V_n^\beta(\omega + i\eta), \qquad (B7)$$

where

$$V_n^\beta(\omega + i\eta) = \langle\phi_n^\beta|\frac{1}{\omega - H_{\text{imp}} + E_g + i\eta}|\phi_1^\beta\rangle \qquad (B8)$$

and $U_n^{\alpha\beta} = \langle\phi_1^\alpha|\phi_n^\beta\rangle$, with $\langle\phi_1^\alpha| = \langle|O_\alpha/\sqrt{\langle|O_\alpha O_\alpha^\dagger|\rangle}$. It is obvious that the main difficulties are to calculate $V_n^\beta(\omega + i\eta)$ in the new basis. By taking advantage of the completeness of $\sum_n |\phi_n^\beta\rangle\langle\phi_n^\beta| = 1$ and the identity

$$\langle\phi_m^\beta|(\omega - H_{\text{imp}} + E_g)\frac{1}{\omega - H_{\text{imp}} + E_g}|\phi_1^\beta\rangle = \delta_{m,1}, \qquad (B9)$$

$V_n^\beta(\omega + i\eta)$ can be obtained through

$$S_{mn}^\beta(\omega + i\eta)V_n^\beta(\omega + i\eta) = E_m, \qquad (B10)$$

where $E_m = \delta_{m,1}$ and $S_{mn}^\beta(\omega + i\eta)$ is a tridiagonal matrix,

$$S_{mn}^\beta(\omega + i\eta) = \begin{bmatrix} \omega - a_1 + E_g + i\eta & -b_2 & 0 & 0 & \cdots \\ -b_2 & \omega - a_2 + E_g + i\eta & -b_3 & 0 & \cdots \\ 0 & -b_3 & \omega - a_3 + E_g + i\eta & -b_4 & \cdots \\ 0 & 0 & -b_4 & \omega - a_4 + E_g + i\eta & \cdots \\ \vdots & \vdots & \vdots & \vdots & \end{bmatrix}, \qquad (B11)$$

where a_n and b_n are the coefficients generated by the Lanczos iterations with the initial configuration $|\phi_1^\beta\rangle$. The linear equations (B10) can be easily solved by the standard library subroutines. Finally, we can obtain the dynamical correlation function $C_{\alpha\beta}^>(\omega + i\eta)$ by solving Eqs. (B7) and (B10). As for $C_{\alpha\beta}^<(\omega + i\eta)$, it can be obtained similarly.

When substituting the Matsubara frequency $i\omega_n$ for the real frequency $\omega + i\eta$ in Eq. (B4), the dynamical correlation functions $C_{\alpha\beta}(i\omega_n)$ on the Matsubara frequency axis can be obtained by following the above two-step procedures, which suggests that ED has direct access to the dynamical quantities on both real- and Matsubara frequency axes. This is in sharp
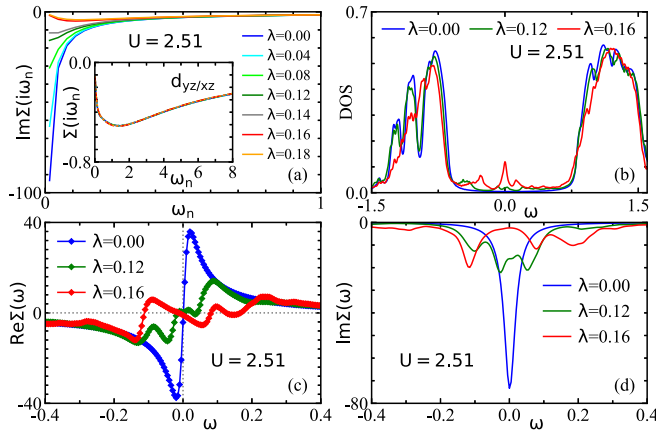
FIG. 7. (a) The influence of spin-orbit coupling on the imaginary part of Matsubara self-energy for the d_{xy} band; that for $d_{yz/xz}$ bands is shown in the inset. (b) Density of states for the d_{xy} band in the Mott ($\lambda = 0.0$), non-Fermi-liquid ($\lambda = 0.12$), and the Fermi-liquid ($\lambda = 0.16$) states. (c) Real and (d) imaginary parts of the self-energy of the d_{xy} band on the real-frequency axis. Here, the electron repulsion is fixed at $U = 2.51$.

contrast to the quantum Monte Carlo, which cannot directly sample the real-frequency dynamical correlations.

APPENDIX C: RESULTS WITH EIGHT BATH SITES COUPLED TO THREE KRAMERS DOUBLETS

In order to further investigate the effect of bath discretization on the OSNFL phase, we have done the DMFT calculations with eight bath sites at zero temperature by using ED as the impurity solver, where four bath sites couple to $|\frac{1}{2}, \pm \frac{1}{2}\rangle$ and $|\frac{3}{2}, \pm \frac{1}{2}\rangle$ Kramers doublets and the remaining four bath sites couple to the $|\frac{3}{2}, \pm \frac{3}{2}\rangle$ doublet. The calculated results at $U = 2.51$ are displayed in Fig. 7, which exhibits distinct characteristics of OSM, OSNFL, and FL phases, similar to those obtained with six bath sites. The OSNFL state can be clearly identified by the imaginary part of the self-energy $\text{Im}\Sigma(i\omega_n)$ on the Matsubara frequency axis. As shown in the inset of Fig. 7(a), $\text{Im}\Sigma_{yz/xz}(i\omega_n)$ for $d_{yz/xz}$ orbitals always extrapolates to zero when ω_n goes to zero, suggesting the typical Fermi-liquid behavior in $d_{yz/xz}$ orbitals. In contrast, at around $\lambda \approx 0.12$, $\text{Im}\Sigma_{xy}(i\omega_n)$ for d_{xy} orbital approaches a finite value at low frequencies, which is different from the divergent behavior for $\lambda < 0.8$ and the tendency towards zero for $\lambda > 0.14$, indicating the occurrence of a breakdown of the Fermi liquid in the d_{xy} orbital due to the finite scattering rate at the Fermi level at zero temperature.

The self-energy $\Sigma_{xy}(\omega)$ on the real-frequency axis further manifests the SOC-induced non-Fermi-liquid nature of the d_{xy} orbital. Figures 7(c) and 7(d) show the real part of the self-energy $\text{Re}\Sigma_{xy}(\omega)$ and the imaginary part of the self-energy $\text{Im}\Sigma_{xy}(\omega)$ at $U = 2.51$ for $\lambda = 0.0$, $\lambda = 0.12$, and $\lambda = 0.16$. For the case of $\lambda = 0.12$, the positive slope of $\text{Re}\Sigma_{xy}(\omega)$ and finite value of $\text{Im}\Sigma_{xy}(\omega)$ at the Fermi level indicate the breakdown of the Fermi liquid at zero temperature. In contrast, the sharp slope of $\text{Re}\Sigma_{xy}(\omega)$ and divergent $\text{Im}\Sigma_{xy}(\omega)$ at $\omega = 0$ suggest a Mott-insulating
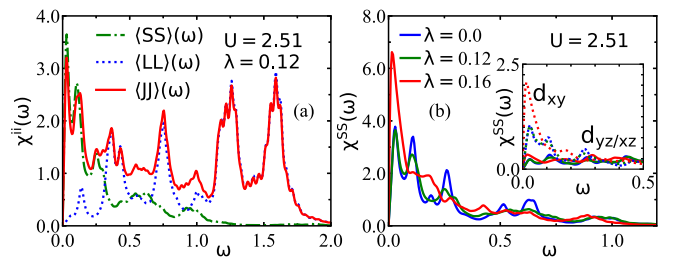

FIG. 8. (a) Dynamical susceptibilities for spin (**S**), orbital (**L**), and total (**J**) angular momenta at $U = 2.51$ and $\lambda = 0.12$. (b) Dynamical spin susceptibilities at $U = 2.51$ for the $\lambda = 0.0$, $\lambda = 0.12$, and $\lambda = 0.16$ cases; the inset shows corresponding orbitally resolved dynamical spin susceptibilities, where solid lines denote $d_{yz/xz}$ orbitals and dashed lines denote the d_{xy} orbital.

state for the $\lambda = 0.0$ case, and the linearly ω dependent $\text{Re}\Sigma_{xy}(\omega)$ and quadratically ω^2 dependent $\text{Im}\Sigma_{xy}(\omega)$ in the vicinity of the Fermi level indicate a typical Fermi-liquid behavior for the $\lambda = 0.16$ case. Figure 7(c) displays the density of states for the d_{xy} orbital in the Mott, non-Fermi-liquid, and Fermi-liquid states at $\lambda = 0.0$, 0.12, and 0.16, respectively.

In order to reveal the mechanism which is responsible for the appearance of the OSNFL state, we have calculated the dynamical susceptibilities $\chi^{ii}(\omega)$, defined by Eqs. (3) and (4), for total spin momentum **S**, total orbital angular momentum **L**, and total angular momentum **J** at $U = 2.51$ and $\lambda = 0.12$, as displayed in Fig. 8(a). The results are similar to that obtained with six bath sites. It is obvious that the low-energy excitations of the total angular momentum **J** are mainly contributed by the spin fluctuations, and the high-energy ones are ascribed to the excitations of the total orbital angular momentum **L**. Since the low-energy excitations were found to dominate the physical properties of the correlated multiorbital systems [52,53], we now pay attention to the low-energy spin fluctuations. Figure 8(b) depicts the spin susceptibilities at $U = 2.51$ for the $\lambda = 0.0$, 0.12, and 0.16 cases. As explained in the main text, at $\lambda = 0.0$, the system is in the OSM state. The appearance of low-energy spin excitations is due to the spins in $d_{yz/xz}$ orbitals screened by their itinerant electrons and the formation of the local triplets with three t_{2g} orbitals filled by four electrons. At $\lambda = 0.16$, the abrupt enhancement in low-energy spin excitations is attributed to the presence of the additional Kondo resonances in the d_{xy} orbital because the spin susceptibilities for $d_{yz/xz}$ orbitals remain almost unchanged, as displayed in the inset of Fig. 8(b). In contrast, at $\lambda = 0.12$, the spin susceptibilities are almost the same as those at $\lambda = 0.0$, indicating the spins in the d_{xy} band do not participate in the Kondo screening. Obviously, the lack of Kondo resonances in the d_{xy} orbital leads to the non-Fermi-liquid behavior.

In addition, we also performed calculations at $U = 3.01$ (not shown) with eight bath sites. The phase transitions from OSM to FL states intermediated by the OSNFL state are detected as a function of SOC, and the distinct characteristics of different phases reflected in the physics quantities like the self-energies, the densities of states, and the dynamical susceptibilities are quite similar to those of the $U = 2.51$ case.

In summary, calculations with eight optimized bath sites indicate that the novel OSNFL state and the phase transitions we obtained with six optimized bath sites are robust and the finite-size effect is negligible.

[1] Y. Kamihara, H. Hiramatsu, M. Hirano, R. Kawamura, H. Yanagi, T. Kamiya, and H. Hosono, Iron-based layered superconductor: LaOFeP, J. Am. Chem. Soc. **128**, 10012 (2006).

[2] Y. Kamihara, T. Watanabe, M. Hirano, and H. Hosono, Iron-based layered superconductor La[$O_{1-x}F_x$]FeAs ($x = 0.05$–0.12) with $T_c = 26$ K, J. Am. Chem. Soc. **130**, 3296 (2008).

[3] W. Witczak-Krempa, G. Chen, Y. B. Kim, and L. Balents, Correlated quantum phenomena in the strong spin-orbit regime, Annu. Rev. Condens. Matter Phys. **5**, 57 (2014).

[4] J. G. Rau, E. Kin-Ho Lee, and H.-Y. Kee, Spin-orbit physics giving rise to novel phases in correlated systems: Iridates and related materials, Annu. Rev. Condens. Matter Phys. **7**, 195 (2016).

[5] C. Martins, M. Aichhorn, and S. Biermann, Coulomb correlations in 4d and 5d oxides from first principles—Or how spin–orbit materials choose their effective orbital degeneracies, J. Phys.: Condens. Matter **29**, 263001 (2017).

[6] Z. Y. Meng, Y. B. Kim, and H.-Y. Kee, Odd-Parity Triplet Superconducting Phase in Multiorbital Materials with a Strong Spin-Orbit Coupling: Application to Doped Sr_2IrO_4, Phys. Rev. Lett. **113**, 177003 (2014).

[7] J. Chaloupka and G. Khaliullin, Doping-Induced Ferromagnetism and Possible Triplet Pairing in d^4 Mott Insulators, Phys. Rev. Lett. **116**, 017203 (2016).

[8] B. J. Kim, H. Ohsumi, T. Komesu, S. Sakai, T. Morita, H. Takagi, and T. Arima, Phase-Sensitive Observation of a Spin-Orbital Mott State in Sr_2IrO_4, Science **323**, 1329 (2009).

[9] J. Chaloupka, G. Jackeli, and G. Khaliullin, Kitaev-Heisenberg Model on a Honeycomb Lattice: Possible Exotic Phases in Iridium Oxides A_2IrO_3, Phys. Rev. Lett. **105**, 027204 (2010).

[10] R. Comin, G. Levy, B. Ludbrook, Z.-H. Zhu, C. N. Veenstra, J. A. Rosen, Y. Singh, P. Gegenwart, D. Stricker, J. N. Hancock, D. van der Marel, I. S. Elfimov, and A. Damascelli, Na_2IrO_3 as a Novel Relativistic Mott Insulator with a 340-meV Gap, Phys. Rev. Lett. **109**, 266406 (2012).

[11] K. W. Plumb, J. P. Clancy, L. J. Sandilands, V. V. Shankar, Y. F. Hu, K. S. Burch, H.-Y. Kee, and Y.-J. Kim, α-$RuCl_3$: A spin-orbit assisted Mott insulator on a honeycomb lattice, Phys. Rev. B **90**, 041112(R) (2014).

[12] S. M. Winter, Y. Li, H. O. Jeschke, and R. Valentí, Challenges in design of Kitaev materials: Magnetic interactions from competing energy scales, Phys. Rev. B **93**, 214431 (2016).

[13] F. Lang, P. J. Baker, A. A. Haghighirad, Y. Li, D. Prabhakaran, R. Valentí, and S. J. Blundell, Unconventional magnetism on a honeycomb lattice in α-$RuCl_3$ studied by muon spin rotation, Phys. Rev. B **94**, 020407(R) (2016).

[14] Y. Zhou, K. Kanoda, and T.-K. Ng, Quantum spin liquid states, Rev. Mod. Phys. **89**, 025003 (2017).

[15] G. Khaliullin, Excitonic Magnetism in Van Vleck–type d^4 Mott Insulators, Phys. Rev. Lett. **111**, 197201 (2013).

[16] T. Sato, T. Shirakawa, and S. Yunoki, Spin-orbital entangled excitonic insulator with quadrupole order, Phys. Rev. B **99**, 075117 (2019).

[17] G. Chen, R. Pereira, and L. Balents, Exotic phases induced by strong spin-orbit coupling in ordered double perovskites, Phys. Rev. B **82**, 174440 (2010).

[18] G. Chen and L. Balents, Spin-orbit coupling in d^2 ordered double perovskites, Phys. Rev. B **84**, 094420 (2011).

[19] O. N. Meetei, W. S. Cole, M. Randeria, and N. Trivedi, Novel magnetic state in d^4 Mott insulators, Phys. Rev. B **91**, 054412 (2015).

[20] L. de' Medici, Hund's coupling and its key role in tuning multiorbital correlations, Phys. Rev. B **83**, 205112 (2011).

[21] A. Georges, Luca de' Medici, and J. Mravlje, Strong correlations from Hund's coupling, Annu. Rev. Condens. Matter Phys. **4**, 137 (2013).

[22] E. Gorelov, M. Karolak, T. O. Wehling, F. Lechermann, A. I. Lichtenstein, and E. Pavarini, Nature of the Mott Transition in Ca_2RuO_4, Phys. Rev. Lett. **104**, 226401 (2010).

[23] J. Mravlje, M. Aichhorn, T. Miyake, K. Haule, G. Kotliar, and A. Georges, Coherence-Incoherence Crossover and the Mass-Renormalization Puzzles in Sr_2RuO_4, Phys. Rev. Lett. **106**, 096401 (2011).

[24] D. Stricker, J. Mravlje, C. Berthod, R. Fittipaldi, A. Vecchione, A. Georges, and D. van der Marel, Optical Response of Sr_2RuO_4 Reveals Universal Fermi-Liquid Scaling and Quasiparticles Beyond Landau Theory, Phys. Rev. Lett. **113**, 087404 (2014).

[25] H. T. Dang, J. Mravlje, A. Georges, and A. J. Millis, Band Structure and Terahertz Optical Conductivity of Transition Metal Oxides: Theory and Application to $CaRuO_3$, Phys. Rev. Lett. **115**, 107003 (2015).

[26] H. T. Dang, J. Mravlje, A. Georges, and A. J. Millis, Electronic correlations, magnetism, and Hund's rule coupling in the ruthenium perovskites $SrRuO_3$ and $CaRuO_3$, Phys. Rev. B **91**, 195149 (2015).

[27] D. Sutter, M. Kim, C. E. Matt, M. Horio, R. Fittipaldi, A. Vecchione, V. Granata, K. Hauser, Y. Sassa, G. Gatti, M. Grioni, M. Hoesch, T. K. Kim, E. Rienks, N. C. Plumb, M. Shi, T. Neupert, A. Georges, and J. Chang, Orbitally selective breakdown of Fermi liquid quasiparticles in $Ca_{1.8}Sr_{0.2}RuO_4$, Phys. Rev. B **99**, 121115(R) (2019).

[28] F. B. Kugler, M. Zingl, H. U. R. Strand, S.-S. B. Lee, J. von Delft, and A. Georges, Strongly Correlated Materials from a Numerical Renormalization Group Perspective: How the Fermi-Liquid State of Sr_2RuO_4 Emerges, Phys. Rev. Lett. **124**, 016401 (2020).

[29] K. Haule and G. Kotliar, Coherence-incoherence crossover in the normal state of iron oxypnictides and importance of Hund's rule coupling, New J. Phys. **11**, 025021 (2009).

[30] Z. P. Yin, K. Haule, and G. Kotliar, Magnetism and charge dynamics in iron pnictides, Nat. Phys. **7**, 294 (2011).

[31] N. Lanatà, H. U. R. Strand, G. Giovannetti, B. Hellsing, L. de' Medici, and M. Capone, Orbital selectivity in Hund's metals: The iron chalcogenides, Phys. Rev. B **87**, 045122 (2013).

[32] M. Yi, D. H. Lu, R. Yu, S. C. Riggs, J.-H. Chu, B. Lv, Z. K. Liu, M. Lu, Y.-T. Cui, M. Hashimoto, S.-K. Mo, Z. Hussain,

C. W. Chu, I. R. Fisher, Q. Si, and Z.-X. Shen, Observation of Temperature-Induced Crossover to an Orbital-Selective Mott Phase in $A_x Fe_{2-y} Se_2$ (A=K, Rb) Superconductors, Phys. Rev. Lett. **110**, 067003 (2013).

[33] P. O. Sprau, A. Kostin, A. Kreisel, A. E. Böhmer, V. Taufour, P. C. Canfield, S. Mukherjee, P. J. Hirschfeld, B. M. Andersen, and J. C. S. Davis, Discovery of orbital-selective Cooper pairing in FeSe, Science **357**, 75 (2017).

[34] A. Koga, N. Kawakami, T. M. Rice, and M. Sigrist, Orbital-Selective Mott Transitions in the Degenerate Hubbard Model, Phys. Rev. Lett. **92**, 216402 (2004).

[35] P. Werner and A. J. Millis, High-Spin to Low-Spin and Orbital Polarization Transitions in Multiorbital Mott Systems, Phys. Rev. Lett. **99**, 126405 (2007).

[36] L. de' Medici, S. R. Hassan, M. Capone, and X. Dai, Orbital-Selective Mott Transition out of Band Degeneracy Lifting, Phys. Rev. Lett. **102**, 126401 (2009).

[37] H. Lee, Y.-Z. Zhang, H. O. Jeschke, and R. Valentí, Orbital-selective phase transition induced by different magnetic states: A dynamical cluster approximation study, Phys. Rev. B **84**, 020401(R) (2011).

[38] Z.-Y. Song, H. Lee, and Y.-Z. Zhang, Possible origin of orbital selective Mott transitions in iron-based superconductors and $Ca_{2-x} Sr_x RuO_4$, New J. Phys. **17**, 033034 (2015).

[39] V. I. Anisimov, I. A. Nekrasov, D. E. Kondakov, T. M. Rice, and M. Sigrist, Orbital-selective Mott-insulator transition in $Ca_{2-x} Sr_x RuO_4$, Eur. Phys. J. B **25**, 191 (2002).

[40] A. Shimoyamada, K. Ishizaka, S. Tsuda, S. Nakatsuji, Y. Maeno, and S. Shin, Strong Mass Renormalization at a Local Momentum Space in Multiorbital $Ca_{1.8} Sr_{0.2} RuO_4$, Phys. Rev. Lett. **102**, 086401 (2009).

[41] M. Neupane, P. Richard, Z.-H. Pan, Y.-M. Xu, R. Jin, D. Mandrus, X. Dai, Z. Fang, Z. Wang, and H. Ding, Observation of a Novel Orbital Selective Mott Transition in $Ca_{1.8} Sr_{0.2} RuO_4$, Phys. Rev. Lett. **103**, 097001 (2009).

[42] L. Huang, L. Du, and X. Dai, Complete phase diagram for three-band Hubbard model with orbital degeneracy lifted by crystal field splitting, Phys. Rev. B **86**, 035150 (2012).

[43] L. Du, L. Huang, and X. Dai, Metal-insulator transition in three-band Hubbard model with strong spin-orbit interaction, Eur. Phys. J. B **86**, 94 (2013).

[44] A. J. Kim, H. O. Jeschke, P. Werner, and R. Valentí, **J** Freezing and Hund's Rules in Spin-Orbit-Coupled Multiorbital Hubbard Models, Phys. Rev. Lett. **118**, 086401 (2017).

[45] R. Triebl, G. J. Kraberger, J. Mravlje, and M. Aichhorn, Spin-orbit coupling and correlations in three-orbital systems, Phys. Rev. B **98**, 205128 (2018).

[46] C. Piefke and F. Lechermann, Rigorous symmetry adaptation of multiorbital rotationally invariant slave-boson theory with application to Hund's rules physics, Phys. Rev. B **97**, 125154 (2018).

[47] A. Georges, G. Kotliar, W. Krauth, and M. J. Rozenberg, Dynamical mean-field theory of strongly correlated fermion systems and the limit of infinite dimensions, Rev. Mod. Phys. **68**, 13 (1996).

[48] R. A. Cooper, Y. Wang, B. Vignolle, O. J. Lipscombe, S. M. Hayden, Y. Tanabe, T. Adachi, Y. Koike, M. Nohara, H. Takagi, C. Proust, and N. E. Hussey, Anomalous criticality in the electrical resistivity of $La_{2-x} Sr_x CuO_4$, Science **323**, 603 (2009).

[49] S. Nakatsuji, D. Hall, L. Balicas, Z. Fisk, K. Sugahara, M. Yoshioka, and Y. Maeno, Heavy-Mass Fermi Liquid near a Ferromagnetic Instability in Layered Ruthenates, Phys. Rev. Lett. **90**, 137202 (2003).

[50] S. Sugano, Y. Tanabe, and H. Kamimura, Multiplets of transition-metal ions in crystals, Pure Appl. Phys. **33**, 1 (1970).

[51] Y. Z. Zhang and M. Imada, Pseudogap and Mott transition studied by cellular dynamical mean-field theory, Phys. Rev. B **76**, 045108 (2007).

[52] Z.-Y. Song, X.-C. Jiang, H.-Q. Lin, and Y.-Z. Zhang, Distinct nature of orbital-selective Mott phases dominated by low-energy local spin fluctuations, Phys. Rev. B **96**, 235119 (2017).

[53] F. B. Kugler, S.-S. B. Lee, A. Weichselbaum, G. Kotliar, and J. von Delft, Orbital differentiation in Hund metals, Phys. Rev. B **100**, 115159 (2019).

[54] H. Park, K. Haule, and G. Kotliar, Cluster Dynamical Mean Field Theory of the Mott Transition, Phys. Rev. Lett. **101**, 186403 (2008).

[55] C. N. Veenstra, Z.-H. Zhu, M. Raichle, B. M. Ludbrook, A. Nicolaou, B. Slomski, G. Landolt, S. Kittaka, Y. Maeno, J. H. Dil, I. S. Elfimov, M. W. Haverkort, and A. Damascelli, Spin-Orbital Entanglement and the Breakdown of Singlets and Triplets in $Sr_2 RuO_4$ Revealed by Spin- and Angle-Resolved Photoemission Spectroscopy, Phys. Rev. Lett. **112**, 127002 (2014).

[56] C. G. Fatuzzo, M. Dantz, S. Fatale, P. Olalde-Velasco, N. E. Shaik, B. Dalla Piazza, S. Toth, J. Pelliciari, R. Fittipaldi, A. Vecchione, N. Kikugawa, J. S. Brooks, H. M. Rønnow, M. Grioni, Ch. Rüegg, T. Schmitt, and J. Chang, Spin-orbit-induced orbital excitations in $Sr_2 RuO_4$ and $Ca_2 RuO_4$: A resonant inelastic x-ray scattering study, Phys. Rev. B **91**, 155104 (2015).

[57] H. Gretarsson, H. Suzuki, H. Kim, K. Ueda, M. Krautloher, B. J. Kim, H. Yavaş, G. Khaliullin, and B. Keimer, Observation of spin-orbit excitations and Hund's multiplets in $Ca_2 RuO_4$, Phys. Rev. B **100**, 045123 (2019).

[58] O. Friedt, M. Braden, G. André, P. Adelmann, S. Nakatsuji, and Y. Maeno, Structural and magnetic aspects of the metal-insulator transition in $Ca_{2-x} Sr_x RuO_4$, Phys. Rev. B **63**, 174432 (2001).

[59] M. Kim, J. Mravlje, M. Ferrero, O. Parcollet, and A. Georges, Spin-Orbit Coupling and Electronic Correlations in $Sr_2 RuO_4$, Phys. Rev. Lett. **120**, 126401 (2018).

[60] G. Zhang and E. Pavarini, Mott transition, spin-orbit effects, and magnetism in $Ca_2 RuO_4$, Phys. Rev. B **95**, 075145 (2017).

[61] B. Burganov, C. Adamo, A. Mulder, M. Uchida, P. D. C. King, J. W. Harter, D. E. Shai, A. S. Gibbs, A. P. Mackenzie, R. Uecker, M. Bruetzam, M. R. Beasley, C. J. Fennie, D. G. Schlom, and K. M. Shen, Strain Control of Fermiology and Many-Body Interactions in Two-Dimensional Ruthenates, Phys. Rev. Lett. **116**, 197003 (2016).

[62] M. E. Barber, A. S. Gibbs, Y. Maeno, A. P. Mackenzie, and C. W. Hicks, Resistivity in the Vicinity of a Van Hove Singularity: $Sr_2 RuO_4$ under Uniaxial Pressure, Phys. Rev. Lett. **120**, 076602 (2018).

[63] Y. S. Lee, J. Yu, J. S. Lee, T. W. Noh, T.-H. Gimm, H.-Y. Choi, and C. B. Eom, Non-Fermi liquid behavior and scaling of the low-frequency suppression in the optical conductivity spectra of $CaRuO_3$, Phys. Rev. B **66**, 041104(R) (2002).

[64] S. Kamal, D. M. Kim, C. B. Eom, and J. S. Dodge, Terahertz-frequency carrier dynamics and spectral weight redistribution in the nearly magnetic metal CaRuO₃, Phys. Rev. B **74**, 165115 (2006).

[65] M. Schneider, D. Geiger, S. Esser, U. S. Pracht, C. Stingl, Y. Tokiwa, V. Moshnyaga, I. Sheikin, J. Mravlje, M. Scheffler, and P. Gegenwart, Low-Energy Electronic Properties of Clean CaRuO₃: Elusive Landau Quasiparticles, Phys. Rev. Lett. **112**, 206403 (2014).

[66] H. F. Yang, C. C. Fan, Z. T. Liu, Q. Yao, M. Y. Li, J. S. Liu, M. H. Jiang, and D. W. Shen, Comparative angle-resolved photoemission spectroscopy study of CaRuO₃ and SrRuO₃ thin films: Pronounced spectral weight transfer and possible precursor of lower Hubbard band, Phys. Rev. B **94**, 115151 (2016).

[67] Y. Liu, H. P. Nair, J. P. Ruf, D. G. Schlom, and K. M. Shen, Revealing the hidden heavy Fermi liquid in CaRuO₃, Phys. Rev. B **98**, 041110(R) (2018).